Title

Self-consistent ion-by-ion growth model for kinetic isotopic fractionation during calcite precipitation

Authors

Nielsen, Laura C

DePaolo, Donald J

De Yoreo, James J

Publication Date

2012-06-01

DOI

10.1016/j.gca.2012.02.009

Self-consistent ion-by-ion growth model for kinetic isotopic fractionation during calcite precipitation

Laura C. Nielsen[1*], Donald J. DePaolo[1,2], James J. DeYoreo[3]

[1]Center for Isotope Geochemistry, University of California-Berkeley, Berkeley, CA, 94720

[2]Lawrence Berkeley National Laboratory, Berkeley, CA, 94720

[3]The Molecular Foundry, Lawrence Berkeley National Laboratory, Berkeley, CA, 94720

[*]corresponding author: lnielsen@berkeley.edu

1. ABSTRACT

Microscopic mechanisms operating at the mineral-aqueous interface control rates of growth and dissolution, isotope fractionation and trace element partitioning during crystal growth. Despite the importance of characterizing surface kinetic controls on isotopic partitioning, no self-consistent microscopic theory has yet been presented which can simultaneously model both mineral growth rate and isotopic composition. Using a kinetic theory for AB or di-ionic crystal growth, we derive a model to predict precipitation rate and isotope fractionation as a function of growth solution oversaturation and solution stoichiometry and apply the theory to calcium isotope fractionation during calcite precipitation.

Our model assimilates the current understanding of surface controlled isotope fractionation with kinetic theories of ion-by-ion mineral growth to predict isotopic partitioning during the growth of ionic crystals. This approach accounts for the effect of solution composition on microscopic mineral surface structure and composition, providing numerous testable hypotheses for growth of sparingly soluble AB crystals such as calcite, namely:

1) Both oversaturation and solution stoichiometry control growth rate and partitioning of isotopes during precipitation;

2) For growth driven primarily by step propagation, distinct expressions describe dislocation- and 2D nucleation-driven growth rates, while the expression for isotope fractionation is the same for both mechanisms;

3) Mineral precipitation occurring via the formation of an amorphous precursor will generate isotope effects that are not compatible with ion-by-ion growth theory and may therefore be excluded from comparison; and,

4) The absolute kinetic limit of isotope fractionation may not be accessible at high

oversaturation due to the formation of amorphous precursors.

Using calcite as a model system, we derive expressions for growth rate and isotopic fractionation as a function of oversaturation and Ca^{2+}:CO_3^{2-} in solution. Increasing oversaturation increases mineral growth rate and drives isotope partitioning towards the kinetic limit, while increasing the concentration of Ca^{2+} relative to CO_3^{2-} at a given oversaturation tends to drive crystal growth towards isotopic equilibrium. These competing effects attenuate the magnitude of isotope fractionations observable in terrestrial environments.

2. INTRODUCTION

Mineral precipitation from aqueous solution is a widely studied process, with direct relevance to aqueous and environmental geochemistry, geobiology, and industry. Macroscopic descriptions of mineral growth and dissolution rate laws abound in the geochemical literature, (e.g. Chou et al., 1989; Zuddas and Mucci, 1994; Zhang and Dawe, 1998; Morse and Arvidson, 2002; Steefel and Maher, 2009), alongside robust microscopic models for mineral precipitation (Burton et al., 1951). Kinetic, mass-dependent fractionation of stable isotopes and disequilibrium trace element partitioning are widely observed during mineral growth (Watson, 1996; Fantle and DePaolo, 2007; Tang et al., 2008b,a). No existing theory links microscopic mineral growth models with macroscopic models of trace element and isotope partitioning during precipitation. In this paper, we derive a self-consistent model for calcite growth that predicts growth rate and isotope fractionation as a function of growth solution composition. The model is applicable to any sparingly soluble di-molecular salt, and may be extended to incorporate the nonlinear effects of trace element incorporation on both growth rate and trace element partitioning.

2.1. Microscopic and macroscopic descriptions of mineral growth

Microscopic models describing mineral growth were initially derived during the 1950s. The seminal Burton, Cabrera, & Frank (1951; BCF) paper details what is now referred to as terrace-ledge-kink (TLK) theory, a thermodynamic description of the microscopic structure of mineral surfaces and classical, dislocation-driven mineral growth. TLK theory has been applied to model mineral growth from aqueous solution in numerous systems, including KH_2PO_4 (KDP) (DeYoreo et al., 1994) and calcite (Teng et al., 1998, 1999, 2000; Larsen

et al., 2010). Application of the TLK model is not strictly valid in the case of relatively insoluble minerals where kink formation is limited by the rate of stable 1D nucleation along the step (DeYoreo et al., 2009); more recent models of kink creation, propagation, and collision (CPC) may be used to quantify kink densities of lower-solubility minerals such as calcite (Zhang and Nancollas, 1990, 1998).

Isotopic and trace element partitioning during mineral growth have been shown to be kinetically controlled, (e.g. Young et al., 2002), and numerous models have been invoked to describe these observations. The mechanistic underpinning of these models varies widely, from processes such as solid state diffusion (Watson, 1996), overprinting of equilibrium partitioning between solvated and mineral ions by kinetic effects (Lemarchand and Wasserburg, 2004), to kinetic separation due to macroscopic ion fluxes in the mineral surface boundary layer (Fantle and DePaolo, 2007; DePaolo, 2011). None of these models is directly tied to the mechanistic models for mineral growth based on TLK theory. Though a dependence of trace element (Nehrke et al., 2007) and isotope (Spero et al., 1997) partitioning on solution stoichiometry has been observed, these observations were not explicitly modeled. No growth rate model has been presented that depends explicitly on either solution stoichiometry or trace element concentration, both of which directly affect mineral growth rates and growth mechanisms (Zhang and Dawe, 1998; Wasylenki et al., 2005; Davis, 2008; Perdikouri et al., 2009; Larsen et al., 2010; Stack and Grantham, 2010).

2.2. Application of growth models to calcite precipitation

Calcium carbonate mineral precipitation has been extensively studied as a model system for both microscopic (Dove et al., 2008; Teng et al., 1998, 2000), and macroscopic

(Zhang and Dawe, 1998; Tang et al., 2008a; DePaolo, 2011) theories for mineral growth and trace element and isotope distribution. Teng et al. (2000) applied BCF theory to calcite precipitation and demonstrated that dislocation-driven spiral growth is the dominant growth mechanism at low thermodynamic driving force (i.e. low oversaturation), while at higher oversaturation, step generation and growth is driven by 2D nucleation. Each growth mechanism is associated with distinct microscopic surface structures and corresponding rate laws: dislocation-driven step growth rate is a linear function of oversaturation as predicted by classical theory, while higher order rate laws, (e.g. Malkin et al., 1989; van der Eerden, 1993; Dove et al., 2008), describe 2D nucleation-driven growth.

Significant variability in the calcium isotope composition of terrestrial and solar system materials including calcite has been observed and attributed to mass-dependent isotope fractionation (Russell et al., 1978; Simon and DePaolo, 2010). Biogenic fractionation during $CaCO_3$ mineralization is an important source of variation: organisms fractionate calcium isotopes during biomineralization of shell (Skulan et al., 1997; Gussone et al., 2003; Chang et al., 2004; DePaolo, 2004; Gussone et al., 2004; Nägler, 2000; Böhm et al., 2006; Hippler et al., 2006, 2009) and bone (Skulan and DePaolo, 1999; DePaolo, 2004; Komiya et al., 2008; Reynard et al., 2010). In all cases, the solid carbonate phase is enriched in the light isotope, typically by $\sim 1-2‰$ relative to the growth medium, strongly suggesting a kinetic effect. Isotopic fractionation of similar magnitude may be generated by inorganic precipitation of calcium carbonate in the lab (Gussone et al., 2003; Lemarchand and Wasserburg, 2004; Gussone et al., 2005). Kinetic fractionation of oxygen isotopes has also been observed during calcite growth (Dietzel et al., 2009; Gabitov et al., 2011). Controlled growth experiments suggest that calcite growth rate is correlated with the magnitude of isotopic

fractionation (Lemarchand and Wasserburg, 2004; Tang et al., 2008a), and various mechanisms have been proposed to explain these observations.

Distribution of trace elements such as Sr, Mg and U during inorganic and biogenic calcite precipitation also varies as a function of growth rate (Tang et al., 2008a) and solution stoichiometry (Russell et al., 2004). Concentrations of trace elements in solution also affects growth rate, so the relationship between trace element incorporation and growth kinetics is nonlinear (Wasylenki et al., 2005). A mechanistic description of trace element partitioning and the effect of trace elements on growth kinetics is currently lacking.

DePaolo (2011) developed a model that describes the calcium isotope fractionation and strontium partitioning observed by Tang et al. (2008 a & b) during inorganic calcite precipitation experiments. This model posits that the relative attachment and detachment fluxes of ions to the growing mineral surface controls the degree to which a mineral isotopic composition reflects equilibrium (α_{eq}) or kinetic (α_f) fractionation endmembers. When the mineral growth rate exceeds the rate of exchange of ions between mineral and aqueous solution, the isotopic composition tends towards α_f. The equilibrium fractionation is expressed only when growth rate is much smaller than the exchange rate. This model does not account explicitly for the effects of changes to solution composition−other than oversaturation−on isotope fractionation, nor does it take into account the dependence on oversaturation of the densities of microscopic features at which attachment and detachment occur. However, the theory is consistent with forward and reverse fluxes of ions governing mineral growth in microscopic models of ionic crystal growth (Zhang and Nancollas, 1998) and accounts for much of the available laboratory data on Ca isotope and Sr/Ca fractionation.

Zhang & Nancollas (1998) detailed a model for ion-by-ion AB (NaCl structure) crystal

growth based on CPC theory, which accounts for the stoichiometry of the growth solution. This model applies a kinetic steady state approach and considers the elementary attachment and detachment of ions to and from the mineral surface (Zhang and Nancollas, 1990). Though the theory was explicitly derived for the (001) face of an AB crystal, Larsen et al. (2010) demonstrated that this theory can accurately predict changes in calcite precipitation rate on the calcite $\{10\bar{1}4\}$ face due to changes in solution stoichiometry, and Wolthers et al. (2012) have recently extended the model to account for solution pH. As with growth rate, the ratio of Ca^{2+} to CO_3^{2-} ions in solution (solution stoichiometry) should affect the ability of the mineral surface to exchange ions with solution. In a calcium rich solution, back reaction of Ca will be promoted, because attachment of carbonate ions becomes the growth rate limiting step. Such exchange must facilitate calcium isotopic equilibration of the mineral surface with aqueous solution, driving the solid away from the kinetic end-member composition. A combination of these two theories, then, may be used to describe isotope partitioning as a function of solution composition during surface-controlled mineral growth.

2.3. Mechanics of AB crystal growth

The surface of a sparingly soluble AB mineral such as calcite in contact with aqueous solution is schematically depicted in Fig. 1. Assuming that the oversaturation is smaller than that at which amorphous precursor phases are generated, mineral growth and dissolution proceed via the advancement and retreat of monomolecular steps across the surface. At very low oversaturations, steps are generated at dislocations on the surface, leading to the formation of growth hillocks (Teng et al., 2000). At higher oversaturations, the ther-

modynamic driving force becomes sufficiently high to cause heterogeneous nucleation on the surface (Teng et al., 2000). The resulting 2D nuclei act as a source of step edges analogous to growth hillocks. The advancement of these steps drives overall mineral growth. In both cases, A and B ion attachment and detachment occur primarily at kink sites along step edges, where a large number of chemical bonds are unsatisfied. If, as in calcite, an individual growth unit is a molecule, the step edge orientation may affect its structure and therefore the energetics of bond formation and breaking. On the primary cleavage face of calcite, $\{10\bar{1}4\}$, carbonate ionic units are oriented at an angle to the surface, forming obtuse $(+)$ and acute $(-)$ steps, which travel at different speeds under certain conditions.

[Figure 1 about here.]

2.4. Linking microscopic and macroscopic models of growth

In this paper, we derive a model for growth rate as a function of oversaturation and solution stoichiometry for the cases of spiral dislocation- and 2D nucleation-driven step growth, based on reactions occurring at microscopic step features on the mineral surface. We extend the Zhang $\&$ Nancollas (1998) model of ion-by-ion growth for an AB crystal, allowing for differences in A and B ion attachment and detachment kinetics and introducing a third component A' into the kinetic theory. This derivation can describe the step velocity anisotropy of acute and obtuse faces of spiral growth hillocks observed in calcite. Exchange of ions between mineral kink sites and aqueous solution dictates the final trace element and isotopic composition of the mineral, so we extend this model for the first time to describe isotopic partitioning during surface controlled mineral growth.

Using the framework developed by DePaolo (2011), we derive a general analytical ex-

pression for isotopic fractionation during AB mineral growth as a function of oversaturation and solution stoichiometry. The model accurately describes mass-dependent fractionation of Ca isotopes during calcite growth. Growth rate is considered in two cases: dislocation-driven (spiral) growth, and 2D nucleation-driven growth. The process of ion attachment and detachment at kinks along step edges governing ion incorporation along steps is the same in both cases. Isotopic fractionation during precipitation, α_p, is derived from an expression for step velocity which applies to both spiral and 2D nucleation-driven growth, so a single expression for α_p is needed. Trace element incorporation affects both surface kink density and growth kinetics, whereas isotopic exchange with solution does not. Trace element incorporation will not be addressed in detail here.

We demonstrate that 2D nucleation explains the high order dependence of growth rate on oversaturation observed in inorganic calcite growth experiments reported by Tang et al. (2008), and we also show that our expression for isotope fractionation is consistent with reported $\Delta^{44/40}$Ca values. As a consequence of the microscopic nature of this derivation, we also conclude that our model is not valid for describing growth from highly oversaturated solutions, where calcite grows by the formation of amorphous calcium carbonate (ACC), which then reorganizes to form a crystalline phase. Formation of ACC may be invoked to explain the rate dependence of Ca isotope fractionation during calcium carbonate growth obtained by Lemarchand et al. (2004) and Gussone et al. (2003), which has an inverse growth rate dependence compared with the Tang et al. (2008) data modeled here. The growth solutions used by Gussone et al. (2003) and Lemarchand et al., (2004) are all significantly oversaturated with respect to ACC (solubility reported in Clarkson et al. (1992)), while none of the Tang et al. (2008) solution compositions exceed this solubility threshold.

The results of the former two groups are likely due to the mixing of calcite formed via the ACC pathway and that formed by ion-by-ion addition. For a description of the variables used in the following sections, we refer the reader to Appendix A.

3. SPIRAL GROWTH OF NON-KOSSEL AB CRYSTALS

3.1. Rate of ion incorporation and exchange

The growth of an AB crystal may be modeled by quantifying the relative rates of ion incorporation and back exchange with solution. For a two-component mineral with an NaCl structure growing via dislocation-driven step growth (spiral growth) from aqueous solution, the net rate of ion incorporation depends on the difference of ion fluxes to (R_f) and from (R_b) the mineral surface,

$$R_{net} = R_f - R_b = \frac{\rho u h b d}{y_0}, \tag{3.1}$$

where ρ is kink density (unitless) or the probability of a given site being a kink site, u is the net overall kink propagation rate (s^{-1}), h is the unit step height (m), d is the solid phase density (mol/m^3), b is kink depth (m), and y_0 is the step spacing (m). The total rate of A and B attachment to the surface is $R_f = R_A^f + R_B^f$ ($\frac{mol}{m^2 s}$), and the rate of detachment from the surface is $R_b = R_A^b + R_B^b$ in the same units. For component A,

$$R_A^{net} = R_A^f - R_A^b \tag{3.2}$$

Based on mineral surface geometry, the net rate of surface normal mineral growth due to A incorporation ($\frac{mol}{m^2 s}$) is equal to:

$$R_A^{net} = \frac{\rho u_A^{net} hbd}{y_0} = \frac{v_{st} bd}{2y_0} \tag{3.3}$$

where u_i^{net} is the rate of kink propagation for ion i (s^{-1}), and v_{st} is the lateral step velocity (m/s). Kink density ρ is defined as a/x_0, where x_0 (m) is the average distance between kink sites along a step, and a is the intermolecular distance along the step (m). Rate of kink propagation, u_{net}, is the net frequency of attachment of ions to a kink site. Step spacing or terrace width may be expressed as $y_0 = 4\Gamma L_c$ for a symmetrical growth hillock (Teng et al., 2000), where Γ is approximately equal to 1 for calcite and L_c is critical step length,

$$L_c = \frac{2h|\vec{a} \times \vec{b}|\alpha}{kT\sigma}, \tag{3.4}$$

which depends on step edge free energy per unit step height α (J/m^2), the Boltzmann constant k (J/K), temperature T (K), and oversaturation $\sigma = ln(IAP/K_{sp})$. Ion activity product, $IAP = [A][B]$, is the product of A and B activities in solution. Asymmetrical growth hillocks may be generated in minerals such as calcite by growth rate anisotropy, where obtuse and acute step velocities are not equal (see Appendix C). The rate formulation presented here assumes that all ion attachment and detachment occurs at kink sites and that 2D nucleation is insignificant (Zhang and Nancollas, 1998).

Assuming an A ion can only be added to a B kink site and removed from an A site (e.g.

Fig. 1), the rate of A kink propagation may be written

$$u_A = u_A^f - u_A^b \tag{3.5}$$

where the frequency of A detachment from A kink sites with detachment rate constant ν_A (s^{-1}) is equal to

$$u_A^b = \nu_A P_A, \tag{3.6}$$

and the frequency of A addition to B kinks with attachment rate constant k_A ($s^{-1}M^{-1}$) is equal to

$$u_A^f = k_A[A]P_B, \tag{3.7}$$

where P_A and P_B are the probability of a given kink site being an A or B site respectively (Zhang and Nancollas, 1998), and square brackets denote ion activity. The overall kink propagation rate is the sum of A and B net kink propagation rates, $u = u_A + u_B$. All kink sites are either A or B sites, so $P_A + P_B = 1$.

Combining Eqs. 3.3 and 3.5 - 3.7, the forward and back fluxes of A at the surface become:

$$R_A^f = \frac{\rho k_A[A]P_B hbd}{y_0} \tag{3.8}$$

and

$$R_A^b = \frac{\rho \nu_A P_A hbd}{y_0}. \tag{3.9}$$

3.2. Probability of A and B sites on the surface

Net ion fluxes and therefore growth rate depend on the overall kink density, so abundances of A and B kink sites must be determined. During growth or dissolution, the rate of addition of A must always equal that of B to preserve crystal stoichiometry, so

$$u_A = u_B. \tag{3.10}$$

Thus, $k_A[A]P_B - \nu_A P_A = k_B[B]P_A - \nu_B P_B$. Substituting $1 - P_A$ for P_B, we find that the probability that a given kink site is an A or B site respectively is:

$$P_A = \frac{k_A[A] + \nu_B}{k_A[A] + k_B[B] + \nu_A + \nu_B}, \tag{3.11}$$

and

$$P_B = \frac{k_B[B] + \nu_A}{k_A[A] + k_B[B] + \nu_A + \nu_B} \tag{3.12}$$

3.3. Calculation of surface kink density

The balance of kink site formation via 1D nucleation of AB ion pairs and annihilation via kink collision dictates the steady state kink density of the mineral surface. When the rate of 1D nucleation is equal to i, and the kink propagation rate is u,

$$\rho = 2\sqrt{\frac{i}{2u}} \tag{3.13}$$

(Appendix B).

For an AB crystal, Zhang & Nancollas (1998) determined the rate of formation of stable

1D nuclei, i, as a function of solution composition,

$$i_A = 2\exp\left(\frac{-2\epsilon_A}{kT}\right)(S-1)\frac{\nu_B k_A[A]}{k_A[A]+\nu_B}, \tag{3.14}$$

and

$$i_B = 2\exp\left(\frac{-2\epsilon_B}{kT}\right)(S-1)\frac{\nu_A k_B[B]}{k_B[B]+\nu_A}, \tag{3.15}$$

where S is oversaturation defined as S= $\frac{[A][B]}{K_{sp}}$, K_{sp} is the equilibrium solubility, ϵ_j is the kink formation energy of a j kink site (J) and $i = \frac{i_A+i_B}{2}$. Kink formation energy is equal to half the single AB bond energy (Zhang and Nancollas, 1990). Combining Eqs. 3.5 - 3.7 and identical equations for B, kink propagation rate becomes

$$u = \frac{2k_A k_B[A][B] - 2\nu_A\nu_B}{k_A[A]+k_B[B]+\nu_A+\nu_B} \tag{3.16}$$

(Zhang and Nancollas, 1998).

Eqs. 3.13 - 3.16 may be substituted into Eq. 3.13 to calculate kink density along the step:

$$\rho = \left[(S-1)\left(\left[\exp\left(\frac{-2\epsilon_A}{kT}\right)\frac{\nu_B k_A[A]}{\nu_B+k_A[A]}\right] + \left[exp\left(\frac{-2\epsilon_B}{kT}\right)\frac{\nu_A k_B[B]}{\nu_A+k_B[B]}\right]\right) \left(\frac{\nu_A+\nu_B+k_A[A]+k_B[B]}{k_A[A]k_B[B]-\nu_A\nu_B}\right)\right]^{1/2} \tag{3.17}$$

A simplified expression may be found in Zhang & Nancollas (1998), where the attachment and detachment flux constants of A are assumed to equal those of B.

3.4. Growth rate as a function of oversaturation and solution stoichiometry

To obtain growth rate in terms of solution saturation (S) and stoichiometry ($r_a = [A]/[B]$), attachment and detachment fluxes must be recast in terms of S and flux ratio r. As in Zhang & Nancollas (1998), we define flux ratio such that

$$r = \frac{k_A}{k_B} r_a. \tag{3.18}$$

The equilibrium solubility of an AB crystal is defined as $K_{sp} = [A]_{eq}[B]_{eq}$. At equilibrium, the forward and back fluxes of A and B are equal, so $\rho k_A [A]_{eq} P_B = \rho \nu_A P_A$, thus

$$[A]_{eq} = \frac{\nu_A P_A}{k_A P_B}, \tag{3.19}$$

similarly

$$[B]_{eq} = \frac{\nu_B P_B}{k_B P_A}. \tag{3.20}$$

These equations simplify to

$$K_{sp} = \frac{\nu_A \nu_B}{k_A k_B}, \tag{3.21}$$

which is the equilibrium solubility expressed in terms of the forward and backward flux coefficients. By substituting Eq. 3.21 into the standard equation relating S and K_{sp} we obtain an expression for S in terms of the flux coefficients and the aqueous ion concentrations.

$$S = \frac{k_A k_B [A][B]}{\nu_A \nu_B}, \tag{3.22}$$

which then also allows us to write the forward ionic fluxes in terms of S and r as:

$$k_B[B] = \left(S\frac{\nu_A\nu_B}{r}\right)^{1/2}, \tag{3.23}$$

and

$$k_A[A] = \left(S\nu_A\nu_B r\right)^{1/2}. \tag{3.24}$$

The overall precipitation rate, R_{net} may now be expressed in terms of S and r_a by substituting ρ (Eq. 3.17) and u (Eq. 3.16) into Eq. 3.1:

$$R_{net} = \frac{hbd}{y_0}\left\{\left[\left(\exp\left(\frac{-2\epsilon_A}{kT}\right)\frac{\nu_B^{3/2}(S\nu_A r)^{1/2}}{\nu_B + (S\nu_A\nu_B r)^{1/2}}\right) + \left(\exp\left(\frac{-2\epsilon_B}{kT}\right)\frac{\nu_A^{3/2}(S\frac{\nu_B}{r})^{1/2}}{\nu_A + (S\frac{\nu_A\nu_B}{r})^{1/2}}\right)\right]\left[\frac{\nu_A + \nu_B + (S\nu_A\nu_B r)^{1/2} + (S\frac{\nu_A\nu_B}{r})^{1/2}}{\nu_A + \nu_B}\right]\right\}^{1/2} \left[\frac{2\nu_A\nu_B(S-1)}{\nu_A + \nu_B + (S\nu_A\nu_B r)^{1/2} + (S\frac{\nu_A\nu_B}{r})^{1/2}}\right]. \tag{3.25}$$

Step velocity may similarly be written in terms of S and r (i.e. Eq. 3.3):

$$v_{st} = \frac{R_{net}y_0}{bd} = \rho u h. \tag{3.26}$$

The dependence of growth rate, R_{net}, on S and r_a is plotted in Fig. 2. Rate is maximized at high oversaturation and Ca^{2+}:$CO_3^{2-} \sim 1$ when $\nu_A \sim \nu_B$ and $k_A \sim k_B$. Fig. 2 also shows that R_{net} is more strongly dependent on S than on r, but that r can change R_{net} by about a factor of 10 when increased or decreased by 3 orders of magnitude, a range that is accessed in natural aqueous solutions.

[Figure 2 about here.]

The rate of exchange of a given ion between the mineral surface and aqueous solution dictates the ultimate trace element and isotopic composition of the solid phase (DePaolo, 2011). The relative exchange flux for A may be expressed as a function of supersaturation, S, and flux ratio, r (Eq. 3.18), from the ratio of back to forward reaction rates:

$$\frac{R_A^b}{R_A^f} = \frac{\nu_A P_A}{k_A[A]P_B} = \frac{\nu_A}{k_A[A]}\left(\frac{\nu_B + (S\nu_A\nu_B r)^{1/2}}{\nu_A + (S\frac{\nu_A\nu_B}{r})^{1/2}}\right). \tag{3.27}$$

If we assume that the rate coefficients of A and B ion attachment and detachment are equal (e.g. $k_A = k_B$ and $\nu_A = \nu_B$) and substitute Eqs. 3.18, 3.23, and 3.24, Eq. 3.27 reduces to:

$$\frac{R_A^b}{R_A^f} = \frac{1}{\sqrt{Sr_a}}\left(\frac{1+\sqrt{Sr_a}}{1+\sqrt{S/r_a}}\right), \tag{3.28}$$

which is solely dependent on solution composition. The exchange flux of A based on Eq. 3.28 is plotted as a function of oversaturation and solution stoichiometry in Fig.3. High values of R_b/R_f for A promote equilibrium fractionation or partitioning of A isotopes between the solid phase and aqueous solution. Conversely, low values of R_b/R_f drive the mineral-aqueous system towards kinetic control. Decreasing R_b/R_f may be accomplished by increasing oversaturation, because with increasing S, the first term on the right hand side of Eq. 3.28 decreases. Decreasing A:B (r_a) also decreases R_b/R_f, because decreasing r_a simultaneously decreases the numerator and increases the denominator of the term in parentheses of Eq. 3.28 (Fig.3).

[Figure 3 about here.]

In DePaolo (2011), the backward flux R_b is assumed to equal the mineral dissolution rate under infinite undersaturation at appropriate P, T and pH. According to the model presented here, the net detachment flux of A and B varies with both oversaturation S and solution stoichiometry, although R_b is close to the measured calcite dissolution rate under the S and r_a conditions applicable to seawater and to the available laboratory measurements of Ca isotope fractionation (Fig. 4).

[Figure 4 about here.]

4. HIGHER ORDER GROWTH RATES AND NUCLEATION

The derivation presented above for the relationship between R_{net}, S and r_a, for spiral growth must be modified for high oversaturations where the spiral growth mechanism does not operate. With increasing oversaturation, the dominant mechanism of step initiation undergoes a transformation, where steps initially sourced from screw dislocations on the surface begin to nucleate directly on the surface as 2D islands. This transformation is associated with a higher-order dependence of growth rate on oversaturation, (e.g. Teng et al., 2000). Van der Eerden (1993) determined an expression for the rate of surface normal growth (m/s) driven by 2D nucleation:

$$R = 1.137h\left(Iv_{st}^2\right)^{1/3}, \tag{4.1}$$

where h is step height, I is nucleation frequency ($m^{-2}s^{-1}$), and $v = \rho u_{net} b$ is step velocity (m/s). Nucleation frequency may be written

$$I = \beta_{st} \frac{h}{\Omega} \left(\frac{\xi_2 h \sigma}{\pi \Omega} \right)^{1/2} exp\left(\frac{-\Delta G^*}{kT} \right) \tag{4.2}$$

where ξ_2 is an area shape factor, $\sigma = ln(IAP/K_{sp})$, ΔG^* is the excess Gibbs free energy of the critical nucleus relative to an empty terrace, Ω is the growth unit volume (e.g. $\sim hab$), and β_{st} is the step kinetic coefficient (van der Eerden, 1993). The step kinetic coefficient of van der Eerden (1993) depends on step velocity following,

$$\beta_{st} = \frac{v_{st}}{\sigma}. \tag{4.3}$$

This differs from a more typical expression for β_{st}, where the step kinetic coefficient is assumed to be proportional to the difference between the mineral constituent ion concentration in solution and its equilibrium concentration, (e.g. Teng et al., 2000).

Following Van der Eerden (1993), the free energy barrier of forming a critical 2D nucleus depends on oversaturation, the chemical driving force for growth:

$$\Delta G^* = \frac{\xi \Omega \gamma^2}{hkT\sigma}, \tag{4.4}$$

where γ is the average edge free energy of the nucleus in J/m, and $\xi = 2\xi_2/\xi_1^2$ (van der Eerden, 1993). If I^* is the radius of a rhombic critical nucleus, the perimeter of the nucleus is $\sim \xi_1 \times \mathrm{I}^* \simeq 8 \times \mathrm{I}^*$, and the area of the nucleus is $\sim \xi_2 \times \mathrm{I}^{*2} \simeq 4 \times \mathrm{I}^{*2}$. Thus $\xi \simeq 1/8$.

5. TRANSITION FROM STEP GROWTH TO 2D NUCLEATION

At low oversaturations, dislocation driven step growth will control overall growth rate, because the thermodynamic driving force for formation of 2D nuclei is too low. Above a threshold oversaturation, which can be determined by setting Eqs. 3.25 and 4.1 equal, 2D nucleation will drive growth (Fig. 5). The value at which this transition occurs is sensitive to the average edge free energy of the nucleus γ (Eq. 4.4), the kinetic coefficient β_{st} (Eq. 4.2), and the step edge free energy per unit step height α (Eq. 3.4). Typical values for calcite are poorly constrained, because the presence of contaminants could significantly reduce the free energy barrier for 2D nucleation, leading to very low apparent threshold supersaturations. The use of a background electrolyte could also significantly reduce the free energy barrier for nucleation, by decreasing the free energy of the surface via non-specific ion adsorption (Butt et al., 2006). Experiments conducted by Teng et al. (2000) place the transition at around $\sigma \sim 1$ (S=2.7) for calcite, which is considered a lower limit. Fig. 5 gives a graphical illustration of the rates associated with the two growth mechanisms, using the parameters employed in fit B described in section 7.1 below, to fit experiments conducted in the absence of significant background electrolyte (Tang et al., 2008b).

[Figure 5 about here.]

6. OVERSATURATION AND SOLUTION STOICHIOMETRY DEPENDENT ISOTOPE AND TRACE ELEMENT FRACTIONATION

The flux to and from a mineral surface of isotopes substituting for a given constituent ion will depend on the relative abundance of the ion in solution as well as the activation

energy barrier for isotope or trace element addition and removal. Heavy isotopes tend to have higher kinetic activation energy barriers for chemical reactions, so reaction kinetics are expected to be slightly more sluggish. Trace elements of the same charge fit more or less favorably into the crystal lattice depending on ion size and site structure, affecting the kinetics of trace element incorporation and the overall mineral solubility. Isotope substitution into the mineral lattice does not significantly affect the rate coefficients of ion attachment or detachment, so we assume that it has no effect on mineral growth kinetics. Using the formulations for growth rate during dislocation- and 2D nucleation-driven growth, we derive an analytical expression for isotopic partitioning as a function of solution oversaturation and ion activity ratio. This expression applies to both 2D nucleation and dislocation driven-step growth mechanisms, because ion exchange occurs primarily at the step edge in both cases.

During surface-controlled mineral growth, fractionation of rare isotopes of A (A') may be determined from the relative rates of A' incorporation and removal at kink sites during growth. The partitioning associated with each step and with the overall reaction may be expressed:

$$\alpha_{j-i} = \frac{r_j}{r_i} = \frac{R^j_{A'}}{R^j_A}\frac{1}{r_i}, \tag{6.1}$$

where $i \rightarrow j$ is the forward reaction (e.g. attachment, detachment, or net precipitation), $R^j_{A'}$ and R^j_A are the net rates of A' and A reaction respectively, r_j is the [A']:[A] ratio of the product, and r_i is the [A']:[A] ratio of the reactant.

During step propagation, the fractionation factor of isotopes of A during attachment is

$$\alpha_f = \frac{k_{A'}[A']}{k_A[A]}\frac{1}{r_s} = \frac{k_{A'}}{k_A}, \tag{6.2}$$

where $r_s = \frac{[A']}{[A]}$ in solution. The fractionation factor during detachment is

$$\alpha_b = \frac{\nu_{A'} P_{A'}}{\nu_A P_A} \frac{1}{r_x}, \tag{6.3}$$

where r_x is the ratio of heavy to light isotopes incorporated into the crystal bulk. At steady state, the composition of the mineral bulk with N_i moles of i is constant,

$$\frac{dr_x}{dt} = \frac{1}{N_A}\left(\frac{dN_{A'}}{dt} - r_x \frac{dN_A}{dt}\right) = 0. \tag{6.4}$$

The rate of i addition or removal, $dN_i/dt = R^i_{net}$, and $r_x = R^{A'}_{net}/R^A_{net}$ (DePaolo, 2011). To maintain a steady state isotopic composition, the net rate of A and A' addition to the surface must equal the net rate of A and A' addition to the bulk, so r_x is equal to the the net incorporation of A' by B divided by the net incorporation of A by B,

$$r_x = \frac{k_B[B]P_{A'} - \nu_B P_B P_{B-A'}}{k_B[B]P_A - \nu_B P_B P_{B-A}} = \frac{P_{A'}}{P_A}, \tag{6.5}$$

where P_{B-i} is the probability that a given B site is adjacent to an i site. The relation $r_x = P_{A'}/P_A$ holds as long as the attachment and detachment of B ions to and from A sites have the same coefficients, k_B and ν_B, as to and from A' sites, which is only an adequate approximation for isotopic substitution. Invoking this assumption, kink probabilities cancel from expression 6.3, and isotope fractionation during detachment becomes

$$\alpha_b = \frac{\nu_{A'}}{\nu_A}. \tag{6.6}$$

The fractionation factor of A at equilibrium is a function of the attachment and detachment fractionation factors:

$$\alpha_{eq} = \frac{\alpha_f}{\alpha_b} = \frac{k_{A'}\nu_A}{k_A\nu_{A'}}. \tag{6.7}$$

Thus,

$$\nu_{A'} = \frac{\alpha_f}{\alpha_{eq}}\nu_A. \tag{6.8}$$

The total fractionation of A isotopes during precipitation is defined as:

$$\alpha_p = \frac{r_x}{r_s}, \tag{6.9}$$

which leads to the following expression:

$$\alpha_p = \frac{R^{net}_{A'}}{r_s R^{net}_A} = \frac{R^f_{A'} - R^b_{A'}}{r_s(R^f_A - R^b_A)} = \frac{u_{A'}}{r_s u_A}. \tag{6.10}$$

During growth along the step, the rate of A' attachment to the mineral surface may be expressed as:

$$R^f_{A'} = \frac{\rho k_{A'}[A']P_B hbd}{y_0}. \tag{6.11}$$

Similarly, the detachment flux becomes:

$$R^b_{A'} = \frac{\rho \nu_{A'} P_{A'} hbd}{y_0}. \tag{6.12}$$

By substitution, Eq. 6.9 becomes:

$$\alpha_p = \frac{\alpha_f k_A[A]P_B}{k_A[A]P_B + \nu_A P_A\left(\frac{\alpha_f}{\alpha_{eq}} - 1\right)}. \tag{6.13}$$

This expression reduces to the DePaolo (2011) macroscopic model of kinetic isotope fractionation during surface controlled mineral precipitation:

$$\alpha_p = \frac{\alpha_f}{1 + \frac{R_A^b}{R_A^f}\left(\frac{\alpha_f}{\alpha_{eq}} - 1\right)}. \tag{6.14}$$

This equation represents the DePaolo (2011) model, where R_b/R_f may now be expressed explicitly in terms of S and r via Eq. 3.27. Hence, we have arrived at a microscopic description of isotopic partitioning during crystal growth from aqueous solution that takes account of both solution oversaturation and solution stoichiometry.

7. MODEL APPLICATION TO ISOTOPE FRACTIONATION

7.1. Calcium isotope fractionation during calcite growth

The theory derived thus far will now be applied to calcite, where Ca^{2+} and CO_3^{2-} substitute for A and B, and heavy and light isotopes ^{44}Ca and ^{40}Ca replace A' and A respectively. Growth rate and the kinetic isotopic fractionation factor are calculated for a given solution composition based on Eqs. 3.25 and 6.13 respectively.

No coherent set of calcite precipitation experiments provides sufficient information to fit all parameters involved in this model. Free energy parameters α and γ and attachment rate constants likely depend on solution compositional variables such as ionic strength, which

are not directly accounted for, so values obtained under one set of experimental conditions may not be generally applicable. An attempt to fit the dependence of calcium isotope fractionation on calcite growth kinetics is presented here to demonstrate model implementation, and to reveal gaps in experimental data. We do not account for surface speciation of carbonate, which is addressed in Wolthers et al. (2012). As most experimental data modeled here were obtained within a narrow pH range (8.3-9), and the rate coefficient of cation attachment to both dominant types of CO_3^{2-} surface sites (protonated and deprotonated) may be assumed to be approximately equal (Wolthers et al., 2012), surface carbonate speciation should have little effect on kinetic isotope fractionation of calcium or substituting trace elements or isotopes.

Multiple parameters, including the calcite solubility (K_{sp}), density (d), kink height (h), depth (b) and molecular spacing (a), and kink formation energy (ϵ) were taken from the literature (Table 1). Reasonable values for kink formation energy and step edge free energy per unit step height may be derived from Wolthers et al. (2012). We expect these values to vary somewhat with solution composition and experimental setup. The step kinetic coefficient for 2D nucleation driven growth β_{st} was calculated from Eq. 4.3, with step velocity v_{st} determined from Eqs. 3.25 and 3.26. Parameters not available in the literature, or those with literature values inconsistent with observed precipitation rates were fitted. The following procedure was used to fit the experimental growth rate and isotopic data:

1. Fit detachment and attachment rate coefficients ν and k to step velocity data, calculate kink density and propagation rate using Eqs. 3.17 $\&$ 3.16, calculate step velocity using Eq. 3.26, and calculate β_{st} using Eq. 4.3;

2. Fit α_{eq} and α_f to isotopic data, calculate kink site probabilities using Eqs. 3.11 $\&$

3.12, and calculate α_p using Eq. 6.13;

3. Fit step edge free energy per unit step height (α) to spiral growth rate using Eq. 3.25; and

4. Fit edge free energy of the critical nucleus (γ) to rate data, calculate 2D nucleation frequency using Eq. 4.2 & 4.4, and finally calculate the 2D nucleation-driven growth rate using Eq. 4.1.

[Table 1 about here.]

For each step of fitting, constraints on fitted parameters were obtained from the literature where available. The parameters fitted in step (1) can be evaluated from the solution stoichiometry-dependent step velocities of Davis (2008), Perdikouri et al. (2009), and Larsen et al. (2010) (Table 2; Fig. 6). A similar relationship between step velocity and solution stoichiometry was observed by Stack & Grantham (2010). However, we do not attempt to fit their data here, because their observed step velocities suggest that calcite becomes undersaturated at very high and very low Ca^{2+}:CO_3^{2-}. This phenomenon has not been observed elsewhere, and could be attributed to the presence of impurities or to the evolution in solution composition prior to entering the fluid cell.

To fit attachment and detachment rate coefficients, we first assumed that ν_A=ν_B=ν (because the same bond is being broken) and k_A=k_B=k (because ion attachment rate is limited by calcium dehydration either at the surface or in solution). Step velocities were fitted by adjusting a single parameter, k, and solving ν=$\sqrt{k^2 K_{sp}}$ from Eq. 3.21. Step velocities which were maximized at Ca^{2+}:CO_3^{2-} $\neq$ 1 require that $\nu_A \neq \nu_B$ and/or $k_A \neq k_B$. These were fitted by slightly adjusting ν_B and k_B, using Eq. 3.21 as a constraint. Final k and ν

values obtained for Larsen et al. (2010), Perdikouri et al. (2009), and Davis (2008) acute and obtuse step velocities were in reasonable agreement (Table 2).

For step (2) of the fitting procedure, we used the Fantle & DePaolo (2007) estimate of $\alpha_{eq} \sim 1.0000 \pm 0.0001$, to constrain our fitted value (0.9998). We hypothesize that α_f depends on the relative rates of ^{44}Ca and ^{40}Ca ion dehydration. Ongoing work using MD simulations to derive the relative cation desolvation frequencies suggests that the magnitude of these effects could be appropriate to explain the laboratory data (Hofmann et al., 2011). However, for our purposes, $\alpha_f = k_{A'}/k_A$ is fitted without constraint. To determine step edge free energy per unit step height in (3), we use values equal or similar to the value fitted by Teng et al. (2000): $\alpha \sim 1.41$ J/m^2. This parameter exerts a strong control on spiral growth rate. Increasing α shifts the calculated spiral growth rate to lower values (Fig. 5). For the final fitting step (4), γ was adjusted to fit the observed dependence of growth rate on supersaturation, because a 2D nucleation-driven growth mechanism likely dominates over the entire growth rate range reported by Tang et al. (2008a). In theory, edge free energy of the critical nucleus should be close to step edge free energy per unit step height multiplied by step height ($\alpha \times h$), and the fitted value is consistent with this constraint.

[Figure 6 about here.]

[Table 2 about here.]

To illustrate the effects of varying individual parameters on modeling experimental precipitation rate and isotopic data, we present three fits (A, B and C; Table 3; Fig. 7) to the rate dependence of calcium isotope fractionation reported by Tang et al. (2008). Fits A and B use the attachment and detachment rate constants fitted to Larsen et al. (2010) obtuse step

velocities, while fit C uses exchange coefficients fitted to Davis (2010) obtuse step speeds (Table 2). The kinetic endmember isotopic fractionation factor depends exclusively on exchange coefficients, so A and B use the same fitted value for $\alpha_f = 0.9920$, while the value used in fit C substantially differs $\alpha_f = 0.9963$. Obtuse step velocities were fitted here, because at high Ca^{2+}:CO_3^{2-}, obtuse steps tend to propagate much faster than acute steps and should therefore dominate the isotopic signature. Because isotopic compositions specific to the vicinal faces of calcite are not available, attempting to fit the data using an expression for isotope fractionation incorporating both step types (Appendix C) would introduce further parameters without significantly promoting our understanding of the system.

Using fit A parameters, we found that it is not possible to generate growth rates as low as those observed by Tang et al. (2008) at the lowest supersaturations via the spiral growth mechanism. To correct this discrepancy, we adjusted step edge free energy per unit step height α in fits B and C to a value sufficiently high such that modeled spiral growth rates do not exceed the slowest growth rates reported by Tang et al. (2008) at low oversaturation (Fig. 7b; Table 3). The value for edge work calculated based on this fitted α exceeds the range of values presented by Wolthers et al. (2012) by a factor of ~ 2.

[Table 3 about here.]

[Figure 7 about here.]

7.1.1. Carbon and oxygen isotope fractionation during calcite growth

As presented, the model should be applicable to characterizing isotopic fractionation during the attachment of anions to the mineral surface. In the case of calcite, the proposed rate limiting mechanism for ion attachment to kink sites on the surface is the dehydration

of the cation, both in solution and on the mineral surface. Thus, any difference in rates of CO_3^{2-} dehydration caused by mass differences should be overprinted by the rates of calcium kink dehydration, so the kinetic endmember fractionation factor for both C and O is expected to equal the equilibrium fractionation factor between carbonate adsorbed to calcite as an outer-sphere complex and aqueous CO_3^{2-}. Rate dependent fractionation may still arise if the detachment of carbonate containing heavy C or O is slower than that of carbonate containing light C or O. Inorganic calcite precipitation experiments have yielded conflicting results concerning the growth rate dependence of oxygen isotope fractionation, with some groups observing no dependence (Romanek et al., 1992; Kim and O'Neil, 1997) and others observing a significant growth rate effect (Dietzel et al., 2009; Gabitov et al., 2011). At present, it is unclear whether the carbonate ion mass has any effect on the frequency of detachment. Studies in which growth-rate dependent O isotope fractionation is evident (e.g. Dietzel et al., 2009) must be scrutinized to rule out the effects of isotopic disequilibrium between carbonate species in solution. Solution pH has a large effect on carbonate aqueous speciation, so C and O isotope discrimination between species (e.g. Beck et al., 2005) may be invoked to explain the dependence of C and O isotope fractionation on carbonate concentration during calcite precipitation (Spero et al., 1997). We do not attempt to fit this pH dependence here, because this requires incorporation of the equations derived by Wolthers et al. (2012).

7.1.2. Amorphous precursor formation

Tang et al. (2008) performed precipitation experiments at saturation indices well below the solubility of amorphous calcium carbonate (ACC), so calcite growth in this system

likely occurs primarily by ion-by-ion addition and is therefore adequate for comparison with this model. Based on carbonate concentrations and calcium activities calculated using PHREEQc, the experiments of Lemarchand et al. (2004) and Gussone et al. (2003) were performed at solution supersaturations exceeding the solubility of an amorphous precursor phase (IAP $> 5.9 \times 10^{-7}$) (Clarkson et al., 1992), so they are not expected to be consistent with this model. The observation that the latter two sets of experiments exceeded ACC solubility likely explains why these groups obtain a stable Ca fractionation rate dependence inverse of that reported by Tang et al. (2008).

7.1.3. Implications of solution stoichiometry-dependent isotope fractionation

A key prediction of this model is that the isotopic fractionation factor (and the trace element partition coefficient) should depend on solution stoichiometry as well as on growth rate. We hypothesize that at very high Ca^{2+}:CO_3^{2-} ion activity ratios, isotope fractionation will approach the equilibrium limit, because back exchange with the solution is encouraged by the abundance of calcium surface sites (high $P_{Ca^{2+}}$) and the low [CO_3^{2-}] in solution (Fig. 8). Conversely at very low Ca^{2+}:CO_3^{2-} ion activity ratios, fractionation should approach the kinetic limit. Qualitatively, the effects of varying oversaturation and solution stoichiometry on fractionation factor can be seen in Fig. 8.

7.1.4. Calcite precipitation from seawater

Using the model coefficients from fits A and B, calcite precipitation from average seawater ([Ca^{2+}]$\sim$2e-03 and [CO_3^{2-}]$\sim$4e-06)(Berner, 1965; Russell et al., 2004) is expected to have $\Delta^{44/40}$Ca$= 0.60‰$, while fit C gives $\Delta^{44/40}$Ca$= 0.70‰$, which are slightly smaller than values typically inferred for marine $CaCO_3$ calcium isotopic fractionation, (e.g. Gus-

sone et al., 2004; Fantle and DePaolo, 2007; Nielsen et al., 2011). Biomineralizing organisms increase the oversaturation of seawater to promote carbonate precipitation by active transport of calcium ions through tissue (Böhm et al., 2006) or by modification of seawater pH (Erez, 2003). The difference between observed seawater-biomineral calcium isotope fractionation ($\sim 1.3‰$) and our expected value ($\sim 0.7‰$) may be explained by the biological enhancement of oversaturation, and the corresponding increase in mineralization rate.

Seawater has an average Ca^{2+}:CO_3^{2-} activity ratio of ~ 450, so inorganic calcium carbonate precipitation from seawater is not expected to reflect the kinetic endmember of isotope fractionation. The carbonate ion concentration and therefore solution stoichiometry is highly variable in the ocean, both geographically (Lea et al., 1999) and temporally (Suzuki et al., 1995) due to changes in seawater pH. Diurnal shifts as large as 0.7 pH units have been observed in seawater adjacent to coral reefs (Suzuki et al., 1995; Suzuku and Kawahata, 2004). Such significant changes in seawater r_a may explain observed fine-scale variability in coralline $CaCO_3$ trace element composition (Meibom et al., 2008). Ocean acidification due to the loading of anthropogenic CO_2 in the atmosphere will decrease [CO_3^{2-}] relative to [Ca^{2+}], altering carbonate mineral growth kinetics and corresponding mineral composition. The response of biomineralizing organisms to ocean acidification may be monitored by investigating changes in biomineral isotopic composition.

[Figure 8 about here.]

7.2. Model application to trace element partitioning

The model derived thus far for mineral precipitation rate and tracer partitioning is applicable to quantifying trace element partitioning during surface controlled calcite growth, assuming the trace elements do not affect overall kink density. This assumption is typically invalid, however, because many trace elements such as Sr^{2+} affect both mineral precipitation rate as well as composition (Wasylenki et al., 2005), at least at high Sr/Ca ratios. A series of expressions may be derived to determine growth rate, accounting for the effect of trace element-occupied kinks on overall kink density as well as the exchange rates of all ions. Additional parameters are required for implementing a such a model. For a trace element that substitutes for A (A') these include rate constants specific to B attachment to A' and B detachment from A', assuming the bonding structure of the A' ion does not affect the long-range bonding structure of the mineral, which it most certainly will with significant tracer incorporation. "Trace" elements may substitute into the solid phase up to mole fraction quantities, directly altering the energetics of bonding at the mineral surface. The ultimate consequence is a dependence of ν and k values as well as mineral solubility (K_{sp}) on mineral composition.

Modeling trace element incorporation into calcite in particular is complex, because growth on the $\{10\bar{1}4\}$ face of calcite is comprised of four symmetrically distinct vicinal faces expressing two kink site geometries (i.e. obtuse and acute), which respond differently to changes in solution stoichiometry. At high Ca^{2+}:CO_3^{2-}, the velocity of obtuse steps increases relative to acute step velocity, indicating that the coefficients ν and k differ between $(+)$ and $(-)$ steps. Thus, isotopes or trace elements which partition preferentially into obtuse or acute steps, respectively may not directly obey Eq. 6.13 in bulk.

To illustrate the difficulty of modeling trace element incorporation into calcite, the variability of strontium partitioning may be considered. In particular, Sr^{2+} does not qualitatively follow the partitioning behavior predicted by the model presented for isotopes above. With increasing growth rate, incorporation of strontium into calcite increases, suggesting the kinetic partitioning of strontium is greater than the equilibrium value (Tang et al., 2008b). However, at high Ca^{2+}:CO_3^{2-}, strontium is also more strongly incorporated into the solid phase (Nehrke et al., 2007). We partially attribute this effect to the increasing obtuse step velocity at high Ca^{2+}:CO_3^{2-}, because strontium is preferentially incorporated into obtuse sites (Paquette and Reeder, 1995). The effect of growth rate anisotropy on isotope and trace element partitioning is discussed in Appendix C.

The model presented in this paper may be used as a foundation for understanding the effects of trace element incorporation on both mineral growth rate and partitioning, although the expressions for trace element-dependent precipitation rate and mineral composition are not derived here. We note that available Sr/Ca data were fit successfully by DePaolo (2011) with the simpler model also used for isotopes, but this success may be due to the fact that the experiments modeled were performed under a relatively restricted set of S and r_a conditions.

8. CONCLUSION

The addition of ions to and removal of ions from the mineral surface controls the mineral isotopic composition during growth. By identifying this mechanism and incorporating compositional variability into preexisting rate relations based on this mechanism, we have derived a general, self-consistent model describing precipitation rate and isotopic compo-

sition simultaneously. We have demonstrated that calcite growth rate and calcium isotope fractionation may be modeled, despite uncertainty in appropriate values for model parameters. This model identifies key variables controlling trace element and isotope partitioning into sparingly soluble AB minerals such as calcite and may inform experimental efforts moving forward. Experimental data required for fitting all model parameters include measurement of:

1) step velocity as a function of S and r_a for both obtuse and acute steps,

2) terrace width as a function of S and r_a for dislocation-driven growth,

3) threshold supersaturation for 2D nucleation,

4) nucleation frequency (I) as a function of S, and

5) isotopic and trace element composition of calcite as a function of S and r_a for both obtuse and acute steps.

The potential applications of this model are extensive. Precipitation rate variability may be predicted as a function of solution oversaturation and stoichiometry, which may be useful in the context of reactive transport modeling or when considering the effects of ocean acidification on paleoproxy isotope partitioning into $CaCO_3$. From an engineering standpoint, mineral purity and isotopic composition may be controlled by altering the solution stoichiometry. For addition of trace elements and isotopes that are kinetically inhibited, the A:B ratio in solution may be tuned to optimize mineral composition. The framework presented here may be used in the future to model precipitation rate, taking the effects of trace element substitution on growth kinetics into account. Such a model will supersede the assumption made here, that B ion attachment to and detachment from A and A' sites will express the same attachment and detachment rate coefficients.

Acknowledgements. This work was supported by the Director, Office of Science, Office of Basic Energy Sciences, of the U.S. Department of Energy under Contract No. DE-AC02-05CH11231.

REFERENCES

Beck W.C., Grossman E.L., and Morse J.W. (2005) Experimental studies of oxygen isotope fractionation in the carbonic acid system at 15^o, 25^o and 40^oC. *Geochim. Cosmochim. Acta* **69**(14), pp. 3493–3503.

Berner R.A. (1965) Activity coefficients of bicarbonate, carbonate and calcium ions in sea water. *Geochim. Cosmochim. Acta* **29**, pp. 947–965.

Böhm F., Gussone N., Eisenhauer A., Dullo W.C., Reynaud S., and Paytan A. (2006) Calcium isotope fractionation in modern scleractinian corals. *Geochim. Cosmochim. Acta* **70**(17), pp. 4452–4462.

Burton W.K., Cabrera N., and Frank F.C. (1951) The growth of crystals and the equilibrium structure of their surfaces. *Philos. Tr. R. Soc. A* **243**(866), pp. 299–358.

Butt H.J., Graf K., and Kappl M. (2006) *Physics and Chemistry of Interfaces*. Wiley-VCH, Weinheim.

Chang V.T.C., Williams R.J.P., Makishima A., Belshawl N.S., and O'Nions R.K. (2004) Mg and Ca isotope fractionation during $CaCO_3$ biomineralisation. *Biochem. Bioph. Res. Co.* **323**(1), pp. 79–85.

Chou L., Garrels R.M., and Wollast R.M. (1989) Comparative study of the kinetics and mechanisms of dissolution of carbonate minerals. *Chem. Geol.* **78**, pp. 269–282.

Clarkson J.R., Price T.J., and Adams C.J. (1992) Role of metastable phases in the spontaneous precipitation of calcium-carbonate. *J. Chem. Soc. Faraday T* **88**(2), pp. 243–249.

Davis K. (2008) *Resolving the nanoscale mechanisms of calcite growth from nonstoichiometric and microbial solutions*. Ph.D. thesis, Rice University.

DePaolo D. (2011) Surface kinetic model for isotopic and trace element fractionation during precipitation of calcite from aqueous solutions. *Geochim. Cosmochim. Acta* **75**(4), pp. 1039–1056.

DePaolo D.J. (2004) Calcium isotopic variations produced by biological, kinetic, radiogenic and nucleosynthetic processes. *Rev. Mineral. Geochem.* **55**, pp. 255–288.

DeYoreo J.J., Land T.A., and Dair B. (1994) Growth-morphology of vicinal hillocks on the (101) face of KH2PO4 - from step-flow to layer-by-layer growth. *Phys. Rev. Lett.* **73**(6), pp. 838–841.

DeYoreo J.J., Zepeda-Ruiz L.A., Friddle R.W., Qiu S.R., Wasylenki L.E., Chernov A.A., Gilmer G.H., and Dove P.M. (2009) Rethinking classical crystal growth models through molecular scale insights: consequences of kink-limited kinetics. *Cryst. Growth Des.* **9**, pp. 5135–5144.

Dietzel M., Tang J., Leis A., and Koehler S.J. (2009) Oxygen isotopic fractionation during inorganic calcite precipitation - Effects of temperature, precipitation rate and pH. *Chem. Geol.* **268**(1-2), pp. 107–115.

Dove P.M., Han N., Wallace A.F., and DeYoreo J.J. (2008) Kinetics of amorphous silica dissolution and the paradox of the silica polymorphs. *P. Natl. Acad. Sci.* **105**(29), pp. 9903–9908.

Erez J. (2003) The source of ions for biomineralization in foraminifera and their implications for paleoceanographic proxies. *Reviews in Mineralogy and Geochemistry: Biomineralization* (eds. P. Dove, J.D. Yoreo, and S. Weiner), Mineralogical Society of America, Washington, volume 54, chapter 5, pp. 115–149.

Fantle M. and DePaolo D. (2007) Ca isotopes in carbonate sediment and pore fluid from ODP Site 807A: The Ca2+(aq)-calcite equilibrium fractionation factor and calcite recrystallization rates in Pleistocene sediments. *Geochim. Cosmochim. Acta* **71**(10), pp. 2524–2546.

Frank F.C. (1974) Nucleation-controlled growth on a one-dimensional growth of finite length. *J. Crystal Growth* **22**(3), pp. 233–236.

Gabitov R.I., Schmitt A.K., Watson E.B., McKeegan K.D., and Harrison T.M. (2011) Growth rate effect on oxygen isotopic fractionation between calcite and fluid: In situ data. *Goldschmidt Conf. Abstr.* , p. 878.

Gussone N., Eisenhauer A., Heuser A., Dietzel M., Bock B., Böhm F., Spero H.J., Lea D.W., Bijma J., and Nägler T.F. (2003) Model for kinetic effects on calcium isotope fractionation (δ^{44}Ca) in inorganic aragonite and cultured planktonic foraminifera. *Geochim. Cosmochim. Acta* **67**(7), pp. 1375–1382.

Gussone N., Langer G., Geisen M., Eisenhauer A., and Riebesell U. (2004) Ca isotope fractionation in coccolithophores. *Geochim. Cosmochim. Acta* **68**(11), pp. A207–A207.

Gussone N., Böhm F., Eisenhauer A., Dietzel M., Heuser A., Teichert B.M.A., Reitner

J., Worheide G., and Dullo W.C. (2005) Calcium isotope fractionation in calcite and aragonite. *Geochim. Cosmochim. Acta* **69**(18), pp. 4485–4494.

Hippler D., Eisenhauer A., and Nägler T.F. (2006) Tropical Atlantic SST history inferred from Ca isotope thermometry over the last 140ka. *Geochim. Cosmochim. Acta* **70**(1), pp. 90–100.

Hippler D., Kozdon R., Darling K.F., Eisenhauer A., and Nägler T.F. (2009) Calcium isotopic composition of high-latitude proxy carrier *Neogloboquadrina pachyderma* (sin.). *Biogeosciences* **6**(1), pp. 1–14.

Hofmann A.E., Bourg I.C., and DePaolo D.J. (2011) Ion desolvation as a mechanism for kinetic isotope fractionation. *Goldschmidt Conf. Abstr.* , p. 1035.

Kim S. and O'Neil J.R. (1997) Equilibrium and nonequilibrium oxygen isotope effects in synthetic carbonates. *Geochim. Cosmochim. Acta* **61**(16), pp. 3461–3475.

Komiya T., Suga A., Ohno T., Han J., Guo J., Yamamoto S., Hirata T., and Li Y. (2008) Ca isotopic compositions of dolomite, phosphorite and the oldest animal embryo fossils from the Neoproterozoic in Weng'an, South China. *Gondwana Res.* **14**(1-2), pp. 209–218.

Larsen K., Bechgaard K., and Stipp S.L.S. (2010) Modelling spiral growth at dislocations and determination of critical step lengths from pyramid geometries on calcite surfaces. *Geochim. Cosmochim. Acta* **74**(2), pp. 558–567.

Lea D.W., Bijma J., Spero H.J., and Archer D. (1999) Implications of a carbonate ion effect on shell carbon and oxygen isotopes for glacial ocean conditions. *Use of Proxies*

in Paleoceanography: Examples from the South Atlantic (eds. G. Fischer and G. Wefer), Springer-Verlag, Heidelberg, pp. 513–522.

Lemarchand D. and Wasserburg G. (2004) Rate-controlled calcium isotope fractionation in synthetic calcite. *Geochim. Cosmochim. Acta* **68**(22), pp. 4665–4678.

Malkin A.I., Chernov A.A., and Alexeev I.V. (1989) Growth of dipyramidal face of dislocation-free ADP crystals - Free-energy of steps. *J. Crystal Growth* **97**(3-4), pp. 765–769.

Meibom A., Cuif J.P., Houlbreque F., Mostefaoui S., Dauphin Y., Meibom K.L., and Dunbar R. (2008) Compositional variations at ultra-structure length scales in coral skeleton. *Geochim. Cosmochim. Acta* **72**, pp. 1555–1569.

Morse J.W. and Arvidson R.S. (2002) The dissolution kinetics of major sedimentary carbonate minerals. *Earth-Sci. Rev.* **58**(1-2), pp. 51–84.

Nägler T. (2000) The δ^{44}Ca-temperature calibration on fossil and cultured *Globigerinoides sacculifer*: New tool for reconstruction of past sea surface temperatures. *Geochem. Geophys. Geosys.* **1**.

Nehrke G., Reichart G., Cappellen P.V., Meile C., and Bijma J. (2007) Dependence of calcite growth rate and Sr partitioning on solution stoichiometry: Non-Kossel crystal growth. *Geochim. Cosmochim. Acta* **71**, pp. 2240–2249.

Nielsen L.C., Druhan J.L., Yang W., Brown S.T., and DePaolo D.J. (2011) Calcium isotopes as tracers of biogeochemical processes. *Handbook of Environmental Isotope Geochemistry* (ed. M. Baskaran), Springer, New York, volume 1, chapter 7, pp. 105–124.

Perdikouri C., Putnis C.V., Kasioptas A., and Putnis A. (2009) An atomic force microscopy study of the growth of a calcite surface as a function of calcium/total carbonate concentration ratio in solution at constant supersaturation. *Cryst. Growth Des.* **9**, pp. 4344–4350.

Reynard L.M., Henderson G.M., and Hedges R.E.M. (2010) Calcium isotope ratios in animal and human bone. *Geochim. Cosmochim. Acta* **74**(13), pp. 3735–3750.

Romanek C.S., Grossman E.L., and Morse J.W. (1992) Carbon isotopic fractionation in synthetic aragonite and calcite: Effects of temperature and precipitation rate. *Geochim. Cosmochim. Acta* **235**, pp. 365–370.

Russell A.D., Hönisch B., Spero H.J., and Lea D.W. (2004) Effects of seawater carbonate ion concentration and temperature on shell U, Mg, and Sr in cultured planktonic foraminifera. *Geochim. Cosmochim. Acta* **68**(21), pp. 4347–4361.

Russell W., Papanastassiou D., and Tombrello T. (1978) Ca isotope fractionation on earth and other solar-system materials. *Geochim. Cosmochim. Acta* **42**(8), pp. 1075–1090.

Simon J.I. and DePaolo D.J. (2010) Stable calcium isotopic composition of meteorites and rocky planets. *Earth Planet. Sci. Lett.* **289**(3-4), pp. 457–466.

Skulan J. and DePaolo D.J. (1999) Calcium isotope fractionation between soft and mineralized tissues as a monitor of calcium use in vertebrates. *Proc. Natl. Acad. Sci.* .

Skulan J., DePaolo D.J., and Owens T.L. (1997) Biological control of calcium isotopic abundances in the global calcium cycle. *Geochim. Cosmochim. Acta* **61**(12), pp. 2505–2510.

Spero H.J., Bijma J., Lea D.W., and Bemis B.E. (1997) Effect of seawater carbonate concentration on foraminiferal carbon and oxygen isotopes. *Nature* **390**, pp. 497–500.

Stack A. and Grantham M. (2010) Growth rate of calcite steps as a function of aqueous calcium-to-carbonate ratio: independent attachment and detachment of calcium and carbonate ions. *Cryst. Growth Des.* **10**, pp. 1409–1413.

Steefel C.I. and Maher K. (2009) Fluid-Rock Interaction: A Reactive Transport Approach. *Rev. Mineral. Geochem.* **70**, pp. 485–532.

Suzuki A., Nakamori T., and Kayanne H. (1995) The mechanism of production enhancement in coral reef carbonate systems: model and empirical results. *Sed. Geol.* **99**(3–4), pp. 259–280.

Suzuku A. and Kawahata H. (2004) Reef water CO_2 system and carbon production of coral reefs: Topographic control of system-level performance. *Global Environmental Change in the Ocean and on Land* (ed. M. Shiyomi), Terrapub, pp. 229–248.

Tang J., Dietzel M., Böhm F., Kohler S., and Eisenhauer A. (2008a) Sr^{2+}/Ca^{2+} and $^{44}Ca/^{40}Ca$ fractionation during inorganic calcite formation: II. Ca isotopes. *Geochim. Cosmochim. Acta* **72**, pp. 3733–3745.

Tang J., Köhler S., and Dietzel M. (2008b) Sr^{2+}/Ca^{2+} and $^{44}Ca/^{40}Ca$ fractionation during inorganic calcite formation: I. Sr incorporation. *Geochim. Cosmochim. Acta* **72**, pp. 3718–3732.

Teng H.H., Dove P.M., Orme C.A., and DeYoreo J.J. (1998) Thermodynamics of calcite

growth: Baseline for understanding biomineral formation. *Science* **282**(5389), pp. 724–727.

Teng H.H., Dove P.M., and DeYoreo J.J. (1999) Reversed calcite morphologies induced by microscopic growth kinetics: Insight into biomineralization. *Geochim. Cosmochim. Acta* **63**(17), pp. 2507–2512.

Teng H.H., Dove P.M., and DeYoreo J.J. (2000) Kinetics of calcite growth: Surface processes and relationships to macroscopic rate laws. *Geochim. Cosmochim. Acta* **13**, pp. 2255–2266.

van der Eerden J. (1993) Crystal growth mechanisms. *Handbook of crystal growth* (ed. D.J.T. Hurle), NorthHolland, Amsterdam, volume 1a, pp. 445–447.

Wasylenki L.E., Dove P.M., Wilson D.S., and DeYoreo J.J. (2005) Nanoscale effects of strontium on calcite growth: An in situ AFM study in the absence of vital effects. *Geochim. Cosmochim. Acta* **69**(12), pp. 3017–3027.

Watson E.B. (1996) Surface enrichment and trace-element uptake during crystal growth. *Geochim. Cosmochim. Acta* **60**(24), pp. 5013–5020.

Wolthers M., Nehrke G., Gustafsson J.P., and Cappellen P.V. (2012) Calcite growth kinetics: Modeling the effect of solution stoichiometry. *Geochim. Cosmochim. Acta* **77**, pp. 121–134.

Young E.D., Galy A., and Nagahara H. (2002) Kinetic and equilibrium mass-dependent isotope fractionation laws in nature and their geochemical and cosmochemical significance. *Geochim. Cosmochim. Acta* **66**(6), pp. 1095–1104.

Zhang J. and Nancollas G.H. (1990) Kink densities along a crystal surface step at low temperatures and under nonequilibrium conditions. *J. Crystal Growth* **106**, pp. 181–190.

Zhang J.W. and Nancollas G.H. (1998) Kink density and rate of step movement during growth and dissolution of an AB crystal in a nonstoichiometric solution. *J. Colloid Interf. Sci.* **200**(1), pp. 131–145.

Zhang Y.P. and Dawe R. (1998) The kinetics of calcite precipitation from a high salinity water. *Appl. Geochem.* **13**(2), pp. 177–184.

Zuddas P. and Mucci A. (1994) Kinetics of calcite precipitation from seawater: I. A classical chemical kinetics description for strong electrolyte solutions. *Geochim. Cosmochim. Acta* **58**(20), pp. 4353–4362.

APPENDIX A. VARIABLE INDEX

Variable	Units	Description
a	m	molecular spacing along the step
α	J/m^2	step edge free energy per unit step height
α_b		fractionation factor during detachment
α_{eq}		equilibrium fractionation factor
α_f		fractionation factor during attachment
b	m	kink depth
β_{st}		step kinetic coefficient
ΔG^*	J	Gibbs free energy of the critical nucleus
d	mol/m^3	solid density
ϵ_j	J	kink site formation energy
γ	J/m	edge free energy of the critical nucleus
h	m	step height
I	$m^{-2}s^{-1}$	nucleation frequency
i	s^{-1}	rate of stable kink formation (1D nucleation rate)
K_{sp}		equilibrium solubility
k	J/K	Boltzmann constant
k_j	$s^{-1}M^{-1}$	rate coefficient of j attachment to a kink site
ν_j	s^{-1}	rate coefficient of j detachment from a kink site
ξ_j		2D nucleus shape factor
Ω	m^3	growth unit volume
P_j		probability that a given kink site is a j site
R_i^j	$molm^{-2}s^{-1}$	rate of reaction j for ion i
r		flux ratio
r_a		A:B ion activity ratio (solution stoichiometry)
r_x		isotope ratio of the solution
r_x		isotope ratio of the crystal
ρ		kink density
S		oversaturation (IAP/K_{sp})
σ		supersaturation ($ln(IAP/K_{sp})$)
T	K	temperature
u_j	s^{-1}	propagation rate of kink type j
v_{st}	m/s	lateral step velocity
y_0	m	step spacing or terrace width
$[j]$	M	activity of j in solution

APPENDIX B. KINK DENSITY DERIVATION

To maintain a steady state kink density, kink sites must be annihilated and created at the same rate during mineral precipitation (Frank, 1974; Zhang and Nancollas, 1998). Along a given step length L (m), with average kink spacing x_0 (m), kink propagation rate u (s^{-1}), and molecular unit width a (m), all kinks along L are annihilated by collision in the time (t) required for a given kink to move by x_0. Thus

$$x_0 = uat. \tag{B.1}$$

The total number of kinks is L/x_0, so the frequency of annihilation due to collision(R_{coll}) is

$$R_{coll} = \frac{Lua}{x_0^2}. \tag{B.2}$$

Kinks are simultaneously being created along the step via 1D nucleation, with frequency per molecule i. The rate of kink formation (R_{fm}) is then

$$R_{fm} = 2i\frac{L}{a}, \tag{B.3}$$

where two kinks are created by each nucleation event and L/a is the number of molecules along the step.

At steady state, $R_{coll} = R_{fm}$, so kink density $(\rho = a/x_0)$ may be expressed:

$$\rho = \sqrt{\frac{2i}{u}} = 2\sqrt{\frac{i}{2u}}. \tag{B.4}$$

APPENDIX C. STEP VELOCITY ANISOTROPY

The vicinal faces of calcite display two distinct step edge structures, acute and obtuse. Acute steps form an acute angle with the terrace below, while obtuse steps form obtuse angles. Changing solution stoichiometry and oversaturation shifts the relative growth velocities of acute and obtuse steps, causing the angle (θ) between the faces to change (Fig. 9)(Teng et al., 1999; Larsen et al., 2010). Due to geometric constraints of the calcite $\{10\bar{1}4\}$ face, angle γ between acute-acute and obtuse-obtuse faces is 101.6°. If obtuse step velocity, v_+, is greater than acute step velocity, v_-, θ can be shown to equal:

$$\theta = 2atan\left[tan\left(\frac{\gamma}{2}\right)\frac{v_+ + v_-}{v_+ - v_-}\right]. \tag{C.1}$$

If acute step velocities exceed those of obtuse steps, (v_--v_+) replaces (v_--v_+) in the denominator of Eq. C.1. In time interval t, obtuse and acute steps travel by $v_+t=ny_{0,+}$ and $v_+t=ny_{0,+}$ respectively, where $y_{0,\pm}$ is the step spacing and n is the number of step widths traveled in time t. It is trivial to show that $\frac{v_+}{v_-} = \frac{y_{0,+}}{y_{0,-}}$. The fraction of new growth with obtuse geometry becomes: $f_+=\frac{v_+}{v_+ + v_-}$. By fitting the rate constants k and ν and endmember fractionation factors separately for acute and obtuse faces, independent expressions for step velocity and α_p may be obtained for each step type (Eq. 6.13). The total fractionation factor becomes:

$$\alpha_{p,tot} = f_+\alpha_{p,+} + (1 - f_+)\alpha_{p,-}, \tag{C.2}$$

where $\alpha_{p,\pm}$ is the fractionation factor associated with step type $\pm$.

Unlike trace element or isotopic composition, growth rate is independent of step pro-

portions expressed on the surface, because

$$R_{net} = \frac{vbd}{y_0} = \frac{v_+bd}{y_{0,+}} = \frac{v_-bd}{y_{0,-}}, \tag{C.3}$$

so the solution composition dependence of only a single set of step velocities and terrace widths, acute or obtuse, must be determined experimentally to predict growth rate.

Isotopic fractionation is not expected to vary significantly with step growth anisotropy, because isotope partitioning will not be affected by kink site geometry: isotopes of different mass are similar in size. However, trace elements tend to partition strongly into the acute or obtuse face depending on ionic size, so the total distribution will be sensitive to the growth hillock shape.

[Figure 9 about here.]

LIST OF TABLES

Table 1: Constants applied in all fits to experimental data displayed in Fig. 7. Sources for these constants include Larsen et al. (2010) (ϵ) and Teng et al. (1998) (a, b, h, and K_{sp}).

ϵ/kT	a = 2b (m)	h (m)	d (mol/m^3)	K_{sp}
7.775	$6.4e-10$	$3.1e-10$	27100	$10^{-8.54}$

Table 2: Attachment and detachment frequency rate constants (s^{-1}) fitted to reported step speed data from Davis (2008), Perdikouri et al. (2009), and Larsen et al. (2010) and corresponding oversaturations (S). Kinetic coefficients fitted to obtuse step velocities Larsen (+) and Davis (+) were used in fits A and B and fit C respectively.

Constant	Davis $(+)$	Davis $(-)$	Larsen $(+)$	Larsen $(-)$	Perdikouri
$\nu_{Ca^{2+}}(s^{-1})$	1.70e3	1.14e4	5.64e03	4.60e04	8.38e03
$\nu_{CO_3^{2-}}(s^{-1})$	9.90e3	5.89e2	5.64e03	1.30e03	5.64e03
$k_{Ca^{2+}}(s^{-1}M^{-1})$	6.60e7	4.82e7	1.05e8	2.56e08	4.44e07
$k_{CO_3^{2-}}(s^{-1}M^{-1})$	8.87e7	4.82e7	1.05e8	8.10e07	3.69e08
S	12	12	4.6	4.6	6.3

Table 3: Fitted parameters applied in fits A, B and C displayed in Fig. 7.

Fit	rate constants	α_f	α_{eq}	α (J/m^2)	γ (J/m)
A	Larsen $(+)$	0.9920	0.9998	1.41	1.49e-10
B	Larsen $(+)$	0.9920	0.9998	3.00	1.49e-10
C	Davis $(+)$	0.9963	0.9998	3.00	1.49e-10

LIST OF FIGURES

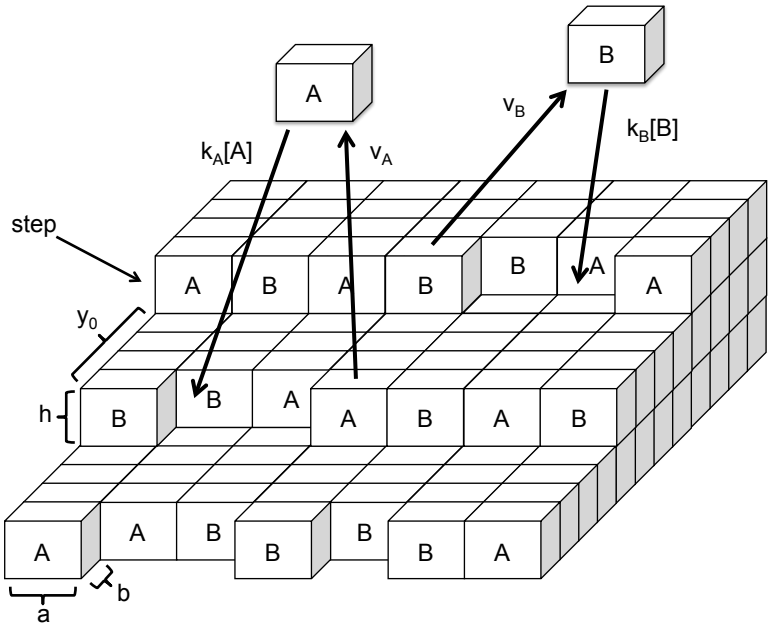

Figure 1: Schematic of kink sites and step edges at the AB mineral surface. A ions in solution exchange with the surface via attachment (with frequency $k_A[A]$ (s^{-1})) and detachment (with frequency ν_A). Step height (h), terrace width (y_0), and molecular unit width (a) are depicted.

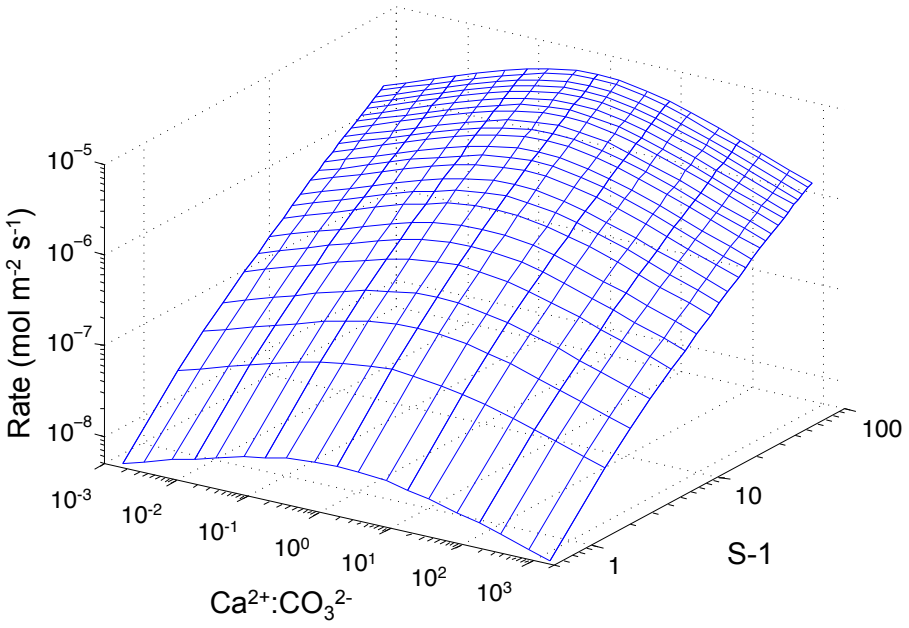

Figure 2: Growth rate modeled as a function of oversaturation, S, and solution stoichiometry based on Eq. 3.25 and parameters used in fit B (see section 7.1). For a given oversaturation, growth rate is greatest at Ca^{2+}:$CO_3^{2-} = 1$, when $\nu_A = \nu_B$ and $k_A = k_B$.

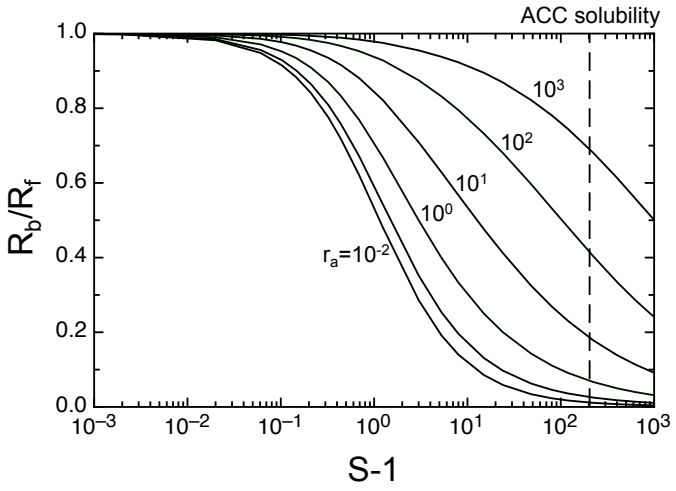

Figure 3: Plot of Ca exchange flux ratio, R_b/R_f (Eq. 3.28), as a function of oversaturation S and the Ca^{2+}:CO_3^{2-} activity ratio in solution (r_a). Increasing S or decreasing r_a will decrease the magnitude of the backward exchange flux (R_b) relative to the forward reaction flux (R_f), driving the system towards kinetically controlled isotope or trace element partitioning. Typical seawater r_a values vary from 10^2 to 10^3. The dashed line indicates where ACC will begin to form. An important feature illustrated here is that the S at which R_b/R_f approaches 1 depends strongly on r_a. Also, the transition from near equilibrium conditions ($R_b >> R_f$) to kinetically controlled conditions ($R_b << R_f$) occurs over a larger range of S as r_a increases. This is a condition that is recognized by DePaolo as being needed to fit available data and is explained here by invoking a microscopic model of crystal growth (DePaolo, 2011).

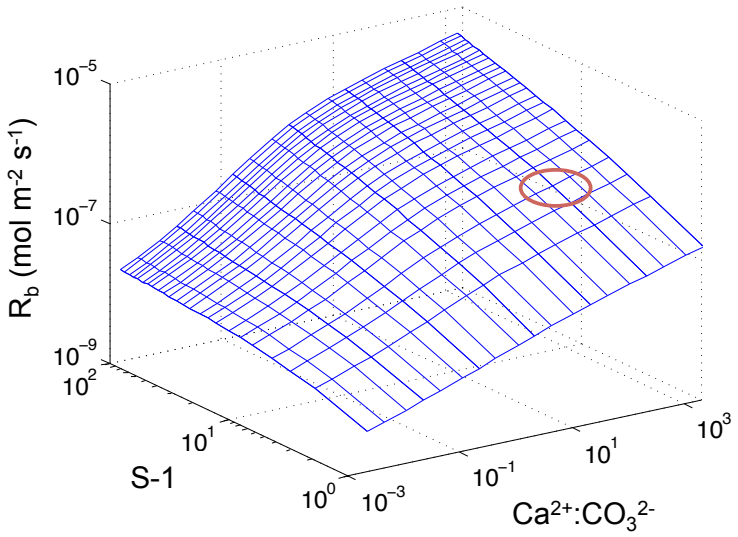

Figure 4: Net ion detachment flux modeled as a function of oversaturation and solution stoichiometry using Eqs. 3.9, 3.4, and 3.17, and fit B parameters (see section 7.1). Oval shows the expected R_b value range for solutions with surface seawater-like values of S and r_a. The expected values are close to the value of 6×10^{-7} mol m^{-2} s^{-1} assumed by DePaolo (2011) to be the value of R_b appropriate to modeling the experiments of Tang et al. (2008).

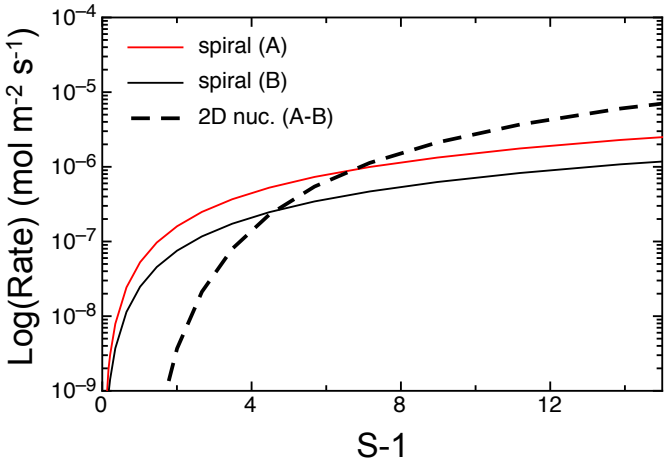

Figure 5: Spiral- and 2D nucleation-driven growth rates (Eqs. 3.25 and 4.1) plotted as a function of oversaturation for model parameters obtained for fits A and B (section 7.1). At low oversaturation, dislocation driven step growth controls growth rate, but above the critical supersaturation (i.e. the intersection of both curves), 2D nucleation controls rate. The transition to 2D nucleation-driven growth occurs at lower supersaturation for fit B, which has a higher step edge free energy per unit step height.

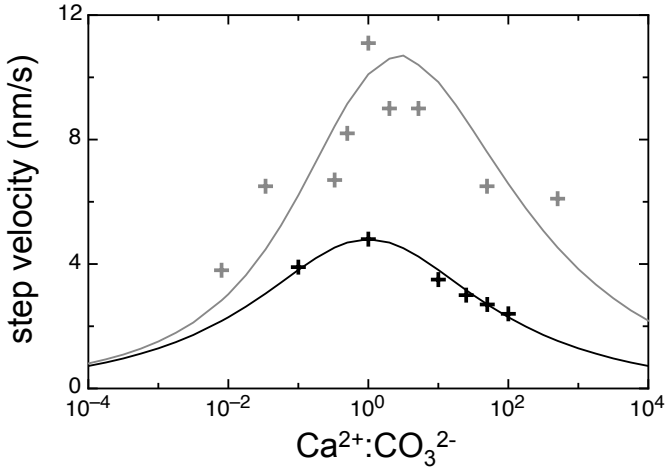

Figure 6: Larsen et al. (2010, black) and Davis (2008, grey) obtuse step velocities plotted as a function of solution stoichiometry (plus symbols) using Eq. 3.26. The model fits to these data are plotted as lines, and the corresponding fitted parameters are listed in Table 2.

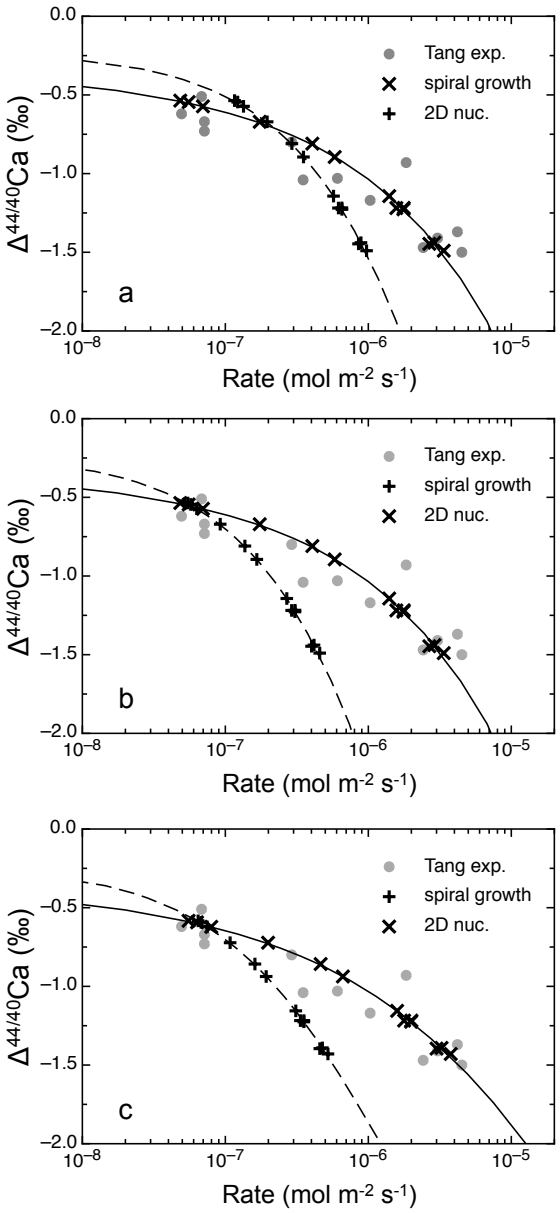

Figure 7: Dislocation- and 2D nucleation driven step growth models using parameters from fits A (a), B (b) and C (c) compared with Tang et al. (2008) experimental data. Rate model fits assuming a spiral growth mechanism are shown as dashed lines, while fits assuming 2D nucleation-driven growth are shown as solid black lines. The experiment-specific modeled data points are shown as black symbols. Tang et al. (2008) experimental rate vs. $\Delta^{44/40}$Ca data are shown as grey circles and are the same in (a-c).

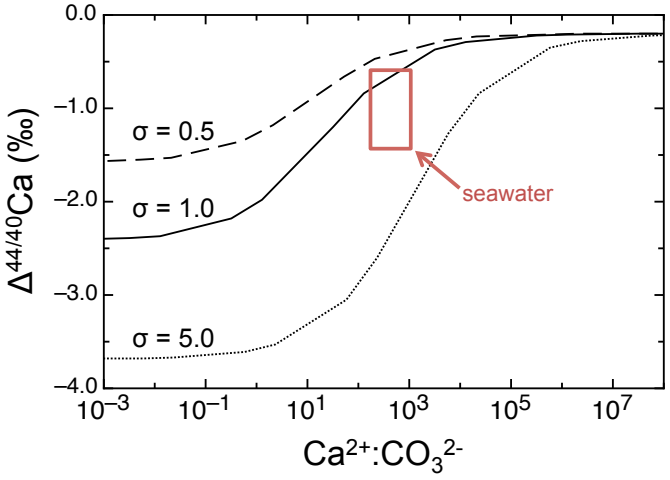

Figure 8: Predicted fractionation dependence on solution stoichiometry at varied solution supersaturations calculated from Eq. 6.13, assuming surface reaction controlled growth using the k and ν values of fits A and B. Rectangle shows approximate expected Ca isotope fractionations for calcite precipitated from surface seawater, or slightly more oversaturated seawater-like solutions.

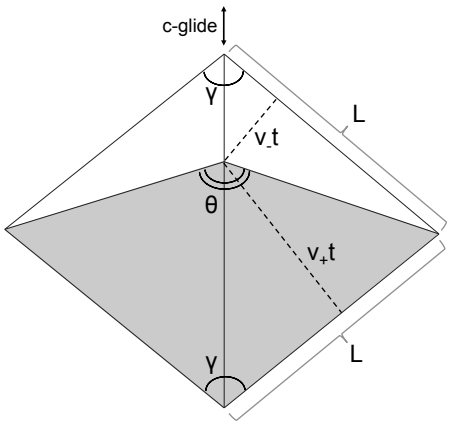

Figure 9: Schematic plan view of a growth hillock under conditions where obtuse (+) faces (shaded) are growing more quickly than acute (-) faces. The angle between similar faces (γ) is 101.6° on the $\{10\bar{1}4\}$ face of calcite. The c-glide plane bisects γ. The step edge length, L, is equal along all faces.